

Inhibiting Analyte Theft in Surface-Enhanced Raman Spectroscopy Substrates: Subnanomolar Quantitative Drug Detection

Bart de Nijs,[†] Cloudy Carnegie,[†] István Szabó,^{‡,§} David-Benjamin Gryns,[†] Rohit Chikkaraddy,^{†,§} Marlous Kamp,[§] Steven J. Barrow,[§] Charlie A. Readman,[§] Marie-Elena Kleemann,[†] Oren A. Scherman,[§] Edina Rosta,^{‡,§} and Jeremy J. Baumberg^{*,†,§}

[†]NanoPhotonics Centre, Cavendish Laboratory, Department of Physics, University of Cambridge, JJ Thompson Avenue, Cambridge CB3 0HE, U.K.

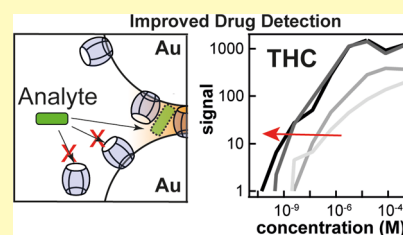
[‡]Department of Chemistry, King's College London, 7 Trinity Street, London SE1 1DB, U.K.

[§]Melville Laboratory for Polymer Synthesis, Department of Chemistry, University of Cambridge, Lensfield Road, Cambridge CB2 1EW, U.K.

Supporting Information

ABSTRACT: Quantitative applications of surface-enhanced Raman spectroscopy (SERS) often rely on surface partition layers grafted to SERS substrates to collect and trap-solvated analytes that would not otherwise adsorb onto metals. Such binding layers drastically broaden the scope of analytes that can be probed. However, excess binding sites introduced by this partition layer also trap analytes outside the plasmonic “hotspots”. We show that by eliminating these binding sites, limits of detection (LODs) can effectively be lowered by more than an order of magnitude. We highlight the effectiveness of this approach by demonstrating quantitative detection of controlled drugs down to subnanomolar concentrations in aqueous media. Such LODs are low enough to screen, for example, urine at clinically relevant levels. These findings provide unique insights into the binding behavior of analytes, which are essential when designing high-performance SERS substrates.

KEYWORDS: SERS, tetrahydrocannabinol, THC, drug detection, self-assembly, nanoparticles, synthetic cannabinoids, spice



Tremendous efforts have been made in the development of surface-enhanced Raman spectroscopy (SERS) substrates, often utilizing colloidal self-assembly or complex patterning of metal surfaces, with many variants that showcase million-fold SERS enhancements factors (EFs).^{1–5} However, because EFs scale as $|E|^4$, spatial inhomogeneities in field enhancement $|E(x,y)|$ result in highly varying Raman intensities across such high-performance substrates.⁶ As a consequence, the majority of the measured SERS spectra are generated by only a small fraction of the molecules, situated in highly localized optically active sites (hotspots)^{1,7–9} (Figure S1). This means that the adsorption location of molecules on SERS substrates greatly affects the strength of their SERS signals. However, because SERS is capable of single-molecule sensing,⁷ as proposed by Le Ru et al., a highly optimized SERS substrate should be able to detect every single molecule at low analyte concentrations.⁹ Local variations can be effectively mitigated by collecting signals over a large number of hotspots, thus averaging SERS intensities for a given analyte concentration.^{10–12} Averaging, however, results in a large fraction of analyte molecules not contributing significantly to the collected SERS spectra. This effect becomes increasingly important at low analyte concentrations when the total number of analyte molecules approaches the (large) number of binding sites available outside the hotspot, resulting in fewer analyte

molecules reaching the high-performance hotspots.^{13,14} Here, this is termed “analyte theft”.

These issues are often ignored when testing novel SERS substrates. Typically, an “optimized” sample is created by coating the substrates with a dense layer of molecules with strong (typically thiol) binding groups with the sole purpose of determining an idealized EF. However, in practice, analytes do not have such strong metal-binding groups, for instance, biomarkers,¹⁵ controlled substances,¹⁶ or other polycyclic aromatic hydrocarbons of interest.^{17,18} Therefore, in addition to reproducible high field enhancements, an ideal SERS substrate should have at least two more features. First, the SERS substrate should have either a specific or ubiquitous affinity to the analyte. A number of SERS substrates have already been presented that employ supramolecular chemistry to capture conventionally nonbinding analytes. Such substrates typically employ biofunctionalization,^{19,20} amphiphilic¹⁵ or hydrophobic²¹ partition layers, or amphiphilic cage constructions such as cyclodextrins^{22–24} or cucurbit[*n*]urils (CB[*n*]s).^{12,25–27} Second, the SERS substrate should preferably only bind analytes near the hotspot to minimize analyte theft. The majority of the proposed substrates, however, are

Received: August 5, 2019

Accepted: September 30, 2019

Published: September 30, 2019

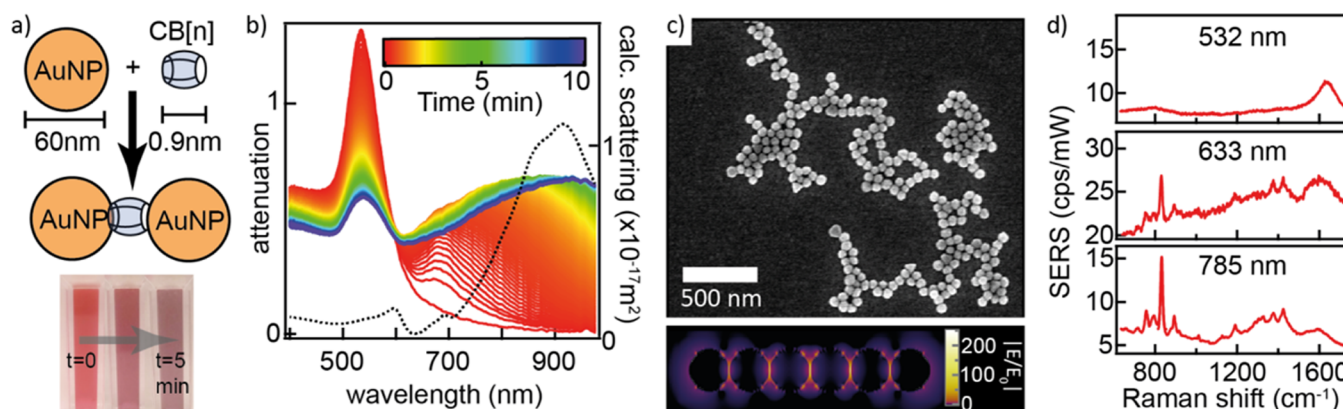


Figure 1. SERS substrate formation and properties. (a) Adding CB[*n*] to a solution of AuNPs (diameter 60 nm) induces aggregation observed as a color change from red to gray, with interparticle spacing of 0.9 nm (the height of the spacer). (b) Extinction spectra of the self-assembly process showing the formation of chain modes in solution over time. Dashed line: finite difference time domain simulated the far-field scattering spectrum for a six-membered AuNP chain. (c) Scanning electron microscopy (SEM) image of AuNP aggregates formed by CB[*n*] self-assembly showing fractal-like structures. Inset: The modeled AuNP chain showing localized hotspots between the nanoparticles with field enhancements $|E/E_0|$ up to 250. (d) SERS spectra from AuNP aggregates under illumination at 532 nm (top), 633 nm (middle), and 785 nm (bottom) in counts per second per milliWatt ($\text{cts}\cdot\text{s}^{-1}\cdot\text{mW}^{-1}$).

fully coated by these receptive partition layers resulting in the number of binding sites approaching or exceeding the total number of analyte molecules available in the system when sensing at submicromolar concentrations (see [Supporting Information](#), Section 2 e.g., calculation). Although several techniques have been introduced to achieve hotspot-selective adsorption,^{9,28–30} no study has focused on how this affects the quantitative sensing of real analytes.

Here, we present a highly reproducible self-assembled SERS substrate consisting of gold nanoparticles and CB[*n*]s as rigid molecular linkers, with a general amphiphilic affinity to analytes. We study quantitatively the effect of eliminating indiscriminant binding on the detection of analytes at submicromolar concentrations. The rigid CB molecular spacer provides precise control over the interparticle spacing in AuNP aggregates,²⁶ and their hydrophobic nature combined with surface-bound charged citrate molecules provides an environment rich in both hydrophilic and hydrophobic sites. In addition, locally replacing the bounding aqueous phase with a neighboring metal nanoparticle surface renders the local chemical environment significantly different from that of a ligand-coated nanoparticle surface. We show that these properties combine to allow for interstitial incorporation of analytes (i.e., outside the CB molecular cavity but within the plasmonic hotspot). We quantitatively demonstrate that by eliminating the indiscriminant binding (analyte theft), this localized interstitial incorporation allows detection of analytes down to subnanomolar concentrations in water. Our results show that this interstitial binding principle can be employed to detect a wide range of analytes as binding does not depend on the analyte's affinity to the metal, but rather on its preference for the amphiphilic interactions presented within the hotspot.

RESULTS AND DISCUSSION

SERS Substrate Formation. To demonstrate interstitial incorporation of analytes and show the benefits of preventing indiscriminate binding, plasmonic substrates consisting of self-assembled AuNPs with a range of molecular spacers of CB[*n*] were compared, where *n* is 5, 6, 7, or 8.²⁵ Adding CB[*n*] to a dispersion of citrate-stabilized AuNPs induces self-assembly, forming aggregates as the particles stick together via the CB[*n*]

which act as rigid 0.9 nm molecular spacers (Figure 1a).^{26,31} This aggregation takes about 10 min during which a gradual color change from red to blue-gray is observed (inset Figure 1a,b). The resulting aggregates consist of a collection of plasmonic hotspots with reproducible localized field enhancements as a result of the rigid sub-nm separations.^{26,32}

SERS Substrate Characterization. Absorbance spectra during aggregation (Figure 1b) show a drop in the single nanoparticle mode (at 534 nm) combined with a rise of the dimer mode (at 690 nm) and chain modes (up to 1000 nm). The red-shifted chain modes visible at the culmination of aggregation result from the coupling together of the individual hotspot modes, feasible only because of the exact reproducibility of the gap spacing. After 10 min, the aggregation is seen to terminate with a predominant scattering mode around 900 nm.^{26,31,33} Scanning electron micrographs of the aggregates (Figure 1c) show a fractal-like structure, with chain lengths between two and seven nanoparticles characteristic for this self-assembly process.^{26,32} Modeling a chain of six 60 nm AuNPs with 0.9 nm spacings using finite difference time domain (FDTD) simulations matches the dominant scattering mode at 900 nm observed in the absorbance experiments (black dashed line, Figure 1b). Plotting the field enhancements of the modeled structure clearly shows that the highest enhancements are localized within the gaps between the nanoparticles.^{34,35} This simplified linear chain is expected to have comparable field enhancements to our aggregates because bends in the chains are found to have limited effects on the resonant localization properties.³² The simulated structure shows field enhancements up to $|E/E_0| = 250$ at 900 nm, which implies EFs around 10^9 when exciting and collecting at resonance.⁶ The broad absorbance spectra in Figure 1b suggest that relatively high EFs are expected over a wide range of wavelengths, from 700 to 1000 nm, though a local maximum is also observed at 534 nm for transverse modes of the chains.

Comparing three different excitation wavelengths (Figure 1d) shows that at 532 nm (transverse mode), no clear SERS signals are observed. For both 633 and 785 nm excitations, the clear peaks seen around 830 cm^{-1} are characteristic for CB[*n*]. The highest emission (in counts per second per milliWatt: $\text{cts}\cdot\text{s}^{-1}\cdot\text{mW}^{-1}$) is observed for 785 nm excitation, as expected from

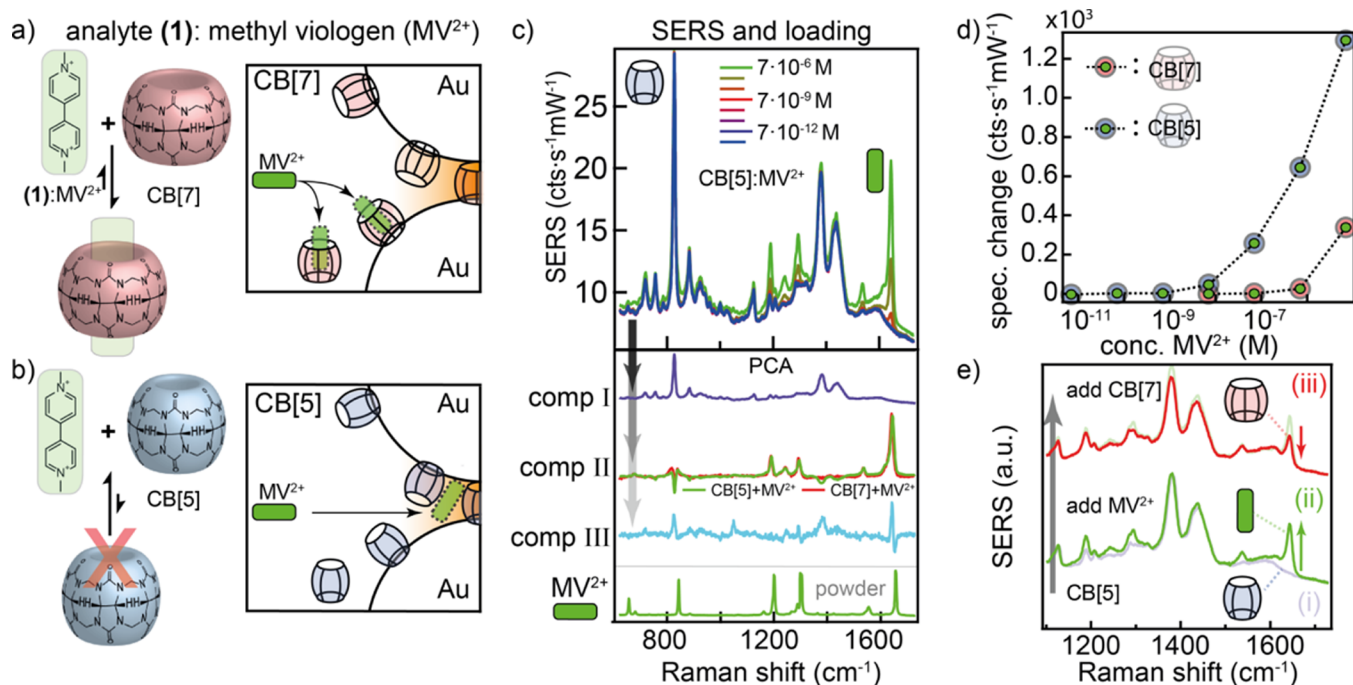


Figure 2. Analyte incorporation mechanisms in plasmonic hotspots. (a) Methyl viologen (MV²⁺) has a strong binding affinity toward CB[7], binding outside the plasmonic hotspots also, effectively lowering the probed MV²⁺ concentration (counter ions have been omitted for clarity). (b) CB[5] is too small to bind MV²⁺ inside, but the constricted hotspot volume (orange shaded) binds analytes interstitially. (c) (Top) SERS spectra for MV²⁺ using CB[5] for different MV²⁺ concentrations down to picomolar. (Bottom) Principal component analysis components from CB[5]:MV²⁺ concentration series, matching CB[5] (comp I) and MV²⁺ bulk Raman (comp II). (d) Integrated spectral changes vs MV²⁺ concentration for AuNP aggregates formed with CB[5] and CB[7]. (e) SERS spectra showing the effect of adding (i) CB[5], then (ii) MV²⁺ resulting in a clear new peak at 1650 cm⁻¹, and subsequently (iii) CB[7], lowering the intensity of the peak at 1650 cm⁻¹ as CB[7] scavenges analytes away from the hotspot.

the absorbance spectra in Figure 1b. Using a 5× microscope objective ensures a large volume of ~10⁷ hotspots are simultaneously probed in solution, providing the averaging as noted above, which is required for reproducible and quantitative SERS spectra.

Analyte Binding Mechanisms. The amphiphilic nature of CB[*n*] allows the larger variants (*n* = 7 and 8) to sequester a range of molecules in their hydrophobic cavity, binding them to the substrate.^{11,12,25} However, we show here that at very small analyte concentrations, binding sites outside the hotspots, arising from excess CB[7,8] molecules in solution and attached to the substrate, scavenge analytes away from the plasmonic hotspots, thus effectively lowering the Raman scattering intensity for a given concentration (Figure 2a, box).

The AuNP metal surfaces are coated with a layer of hydrophobic CB[*n*] molecules (Figure 3), and water, as well as a mixed coating of trisodium citrate (hydrophilic) and citric acid (hydrophilic) used for colloidal charge stabilization.

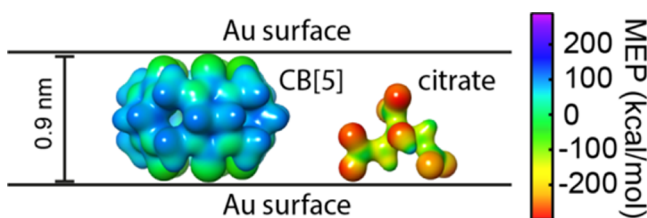


Figure 3. Calculated molecular electrostatic potential maps in implicit water for both CB[5] and citrate showing a strong negative potential for citrate and neutral/positive potential for CB[5].

Bringing two such Au surfaces close together around the hotspot creates a local environment particularly dense in local molecular interactions that no longer resemble a continuous solid–liquid interface. This change in the environment seems to enhance binding of amphiphilic analytes from the aqueous phase because of the close proximity of both hydrophilic and hydrophobic sites (Figure 2b). Such host–guest type of association is similar to that of the CB[7] system (Figure 2a) but instead occurs through interstitial incorporation. When using the smaller CB[5] molecule, size selection prevents the binding of anything larger than methane or methanol inside the small CB volume.^{25,36} This prevents analytes from adsorbing at sites outside the hotspot leaving only the interstitial incorporation mechanism to capture analytes (Figure 2b).

Methyl viologen (MV²⁺) is an amphiphilic analyte too large to fit in CB[5] but with a large affinity to CB[7]. When added to AuNPs aggregated using CB[5] spacers, a set of distinct MV²⁺ peaks appears between 1200 and 1300 cm⁻¹ and at 1650 cm⁻¹, evident from nanomolar concentrations upward, demonstrating interstitial incorporation (Figure 2b, top). This is in line with earlier observations for ethanol/methanol sensing using CB[5].³⁶ PCA is used to isolate the spectral changes and identify their corresponding chemical moieties (Figure 2c, bottom). PCA allows correlated variables (in this case, spectral features) to be identified and through orthogonal transformations to be combined into uncorrelated linear combinations of spectra. These transformed combinations are called principal components (here, referred to as “comp”). The PCA loading plot for comp I closely matches the characteristic CB[5] spectrum in Figure 1d, and comp II can

be closely matched to the powder Raman spectrum of MV^{2+} (bottom trace in Figure 2c). The obtained comp II for CB[5] (green trace) and CB[7] (red trace) are nearly identical, eliminating possible additional differences between the binding mechanisms that could contribute to the EF but which would change the spectral shape or intensity ratios such as analyte orientation or binding into the metal surface (bottom Figure 2c comp II).³⁷

Multiplying the obtained PCA score for comp II with the absolute counts integrated over the full spectral range of the loading plot for comp II provides a measure of the change in the SERS spectra upon MV^{2+} addition in $\text{cts}\cdot\text{s}^{-1}\cdot\text{mW}^{-1}$ (Figure 2d). Comparing the SERS changes between aggregates formed with CB[5] and CB[7] clearly shows stronger spectral peaks for CB[5]. At submicromolar concentrations, changes are visible only for the CB[5] aggregates, showing an improvement in the limit of detection (LOD) by more than an order of magnitude in spite of the smaller spacer's inability to directly bind MV^{2+} . To demonstrate this scavenging effect more clearly, MV^{2+} was added to CB[5]-AuNP aggregates, giving a clear set of SERS peaks (Figure 2e, lower trace), and subsequently CB[7] was added resulting in a reduction of the MV^{2+} peaks (Figure 2e, upper trace). Both experiments confirm that the excess binding sites introduced by CB[7] scavenge analytes away from the hotspots.

Drug Detection. We studied this system in more detail by varying both the CB[*n*] spacer size and the chemical nature of the analyte molecule. To demonstrate that this improvement of LOD is not unique to MV^{2+} and to showcase the robustness of this technique, a set of controlled substances were explored. The chosen substances were selected for their interest in healthcare and substance control, and would typically require at least nanomolar sensitivities to accurately determine their concentrations in urine after consumption.³⁸ Here, we use Δ^9 -THC, the principal psychoactive constituent in cannabis (chemical structure shown in Figure 5a), and several synthetic analogues with different chemical structures designed to induce similar psychotropic effects. Molecular dynamics (MD) simulations were performed using umbrella sampling to model the THC molecule binding into the cavity of the CB[*n*] spacers (Figure 4a). Free energy profiles along the association coordinate were generated as a function of the center-of-mass (COM) distance for each THC-CB[*n*] complex (Figure 4b). This shows that both CB[7] and CB[8] have a highly favorable binding to THC, whereas the binding free energy gain is nearly halved for CB[6] and almost nonexistent for CB[5], showing clearly the effect of reducing the spacer cavity size on analyte binding. We calculate the binding energy for each system from more accurate density functional theory (DFT) calculations (see Methods) to model the interacting complexes, showing that weaker binding affinities are indeed predicted as the size of the spacer is reduced (Figure 5a).

To experimentally probe how these differences in binding affect analyte detection, a concentration series of THC, diluted in methanol, was measured using SERS substrates prepared with each of the different CB[*n*] spacers (Figure 5a,b). A significantly higher analyte component II coefficient for the loading plots was found when using the smaller CB[5] and CB[6] compared to their larger homologues CB[7] and CB[8] with a more rapid increase and higher maximum counts with the same concentration for the smaller spacers. In component III, a range of peaks appear around 1600 cm^{-1} , which we

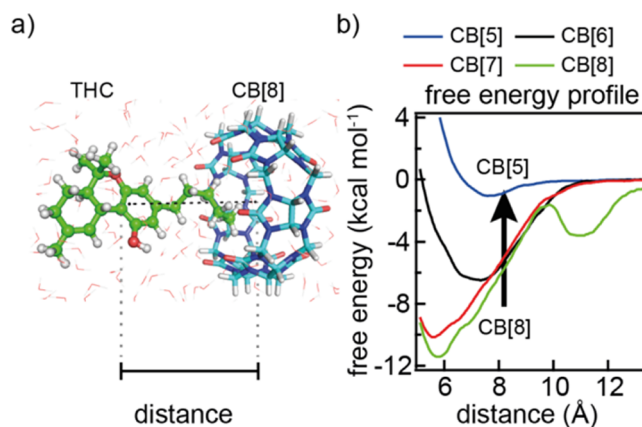


Figure 4. Molecular dynamics simulations of Δ^9 -tetrahydrocannabinol (THC) interacting with different-sized CB[*n*] spacers. (a) Scheme depicting the biasing coordinate used for the umbrella sampling (US) free energy calculations for a THC molecule entering the CB[*n*] cavity, with explicit water. (b) Free energy profiles calculated for each THC-CB[*n*] complex as a function of center-of-mass (COM) distance showing a free energy dip of -9 and -11 kcal mol^{-1} for THC-CB[7] and THC-CB[8] complexes, respectively, decreased binding affinity for CB[6], and no favorable binding free energy for CB[5].

tentatively assign to hydrogen-bonding related interactions (from trisodium citrate, methanol, water, or THC), indicative of analyte binding within the complex environment.³⁶ When comparing the spectral changes for each of the spacers, CB[7] and CB[8] show analyte detection at submicromolar concentrations, but a clear enhancement of spectral changes and lower LOD is observed for CB[5] and CB[6] (Figure 5c), in line with the earlier observations (Figure 2c). This again shows that the analyte is selectively incorporated within the substrate hotspots independent of direct binding within the spacer and that eliminating excess binding improves the detectivity of the THC molecule.

Because the observed interstitial binding is independent of the CB[*n*] spacer cavity at low concentrations, these SERS substrates allow for more ubiquitous analyte incorporation. This makes such substrates a powerful new tool when probing for a range of different analytes such as the many synthetic analogues of THC that have appeared in consumer markets in recent years.^{39–42} To demonstrate that these substrates can indeed incorporate different compounds, a concentration series of three synthetic analogues of THC are also measured (Figure 6a). When comparing the loading plots for each of the compounds, other than the characteristic CB[*n*] peak at 830 cm^{-1} and varying peaks between 1550 and 1700 cm^{-1} , each compound provides a clearly distinct spectrum acting as a unique fingerprint identifier (Figure 6b). The demonstrated nonspecificity to analytes makes this method of sensing highly suitable for routine screening of such compounds. The technique readily copes with rapid changes in chemical structures, required when probing for such compounds.⁴² Comparing the PCA results, it is clear that all compounds can be readily detected at nanomolar concentrations, which is well below typical clinical levels (see Figure 6c).^{38,42,43} To obtain an estimate of the LOD for each compound, a Hill-Langmuir isotherm was fitted to the PCA scores (see Supporting Information, Sections 4–6 for details) using

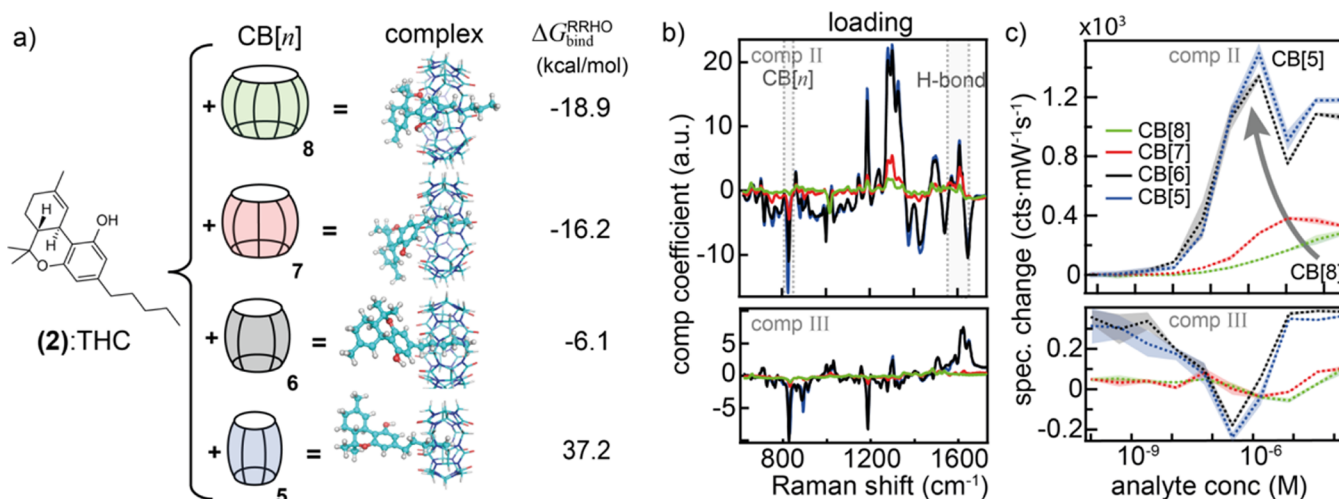


Figure 5. Influence of the analyte binding mechanism on analyte detection. (a) THC binding affinities to each of the CB[n] spacers, modeled using DFT calculations, see [Methods](#) for details. (b) Experimental PCA loading plots from concentration series of each THC–CB[n] complex showing (top) comp II: THC and (bottom) comp III: unassigned molecular interactions. (c) PCA scores for each of the four complexes show an increase in scores (proportional to the signal strength) with decrease in the CB[n] spacer size (arrow).

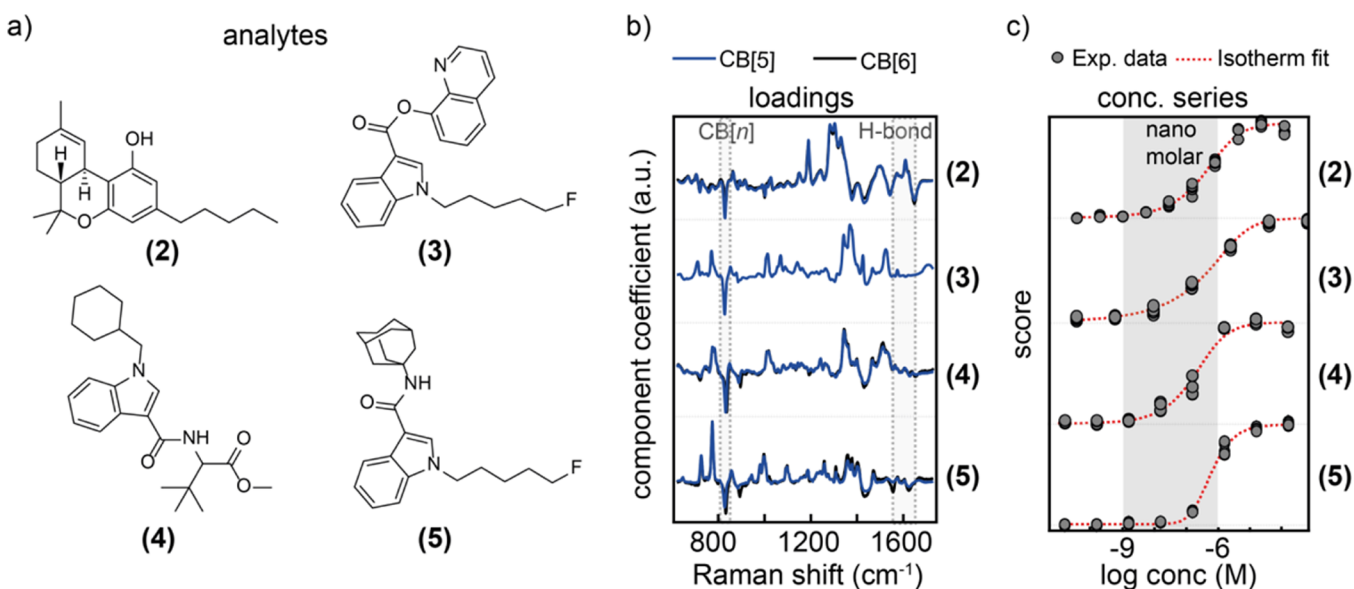


Figure 6. Nonspecific binding of plasmonic hotspots. (a) Four different analytes: THC (2) and three synthetic analogues (3), (4), and (5). (b) PCA loading plots showing distinct spectra for each compound, with little difference whether CB[5] or CB[6] is used. (c) PCA scores and Langmuir isotherm fits for each of the components show LODs clearly in the nanomolar regime with compounds (2–4) showing LODs near or below 1 nanomolar concentration.

$$\text{PCA score} = A \frac{1}{1 + \left(\frac{K_d}{[\text{analyte}]} \right)^N}$$

where A is the saturation value, K_d is the dissociation coefficient, $[\text{analyte}]$ is the analyte concentration, and N is the Hill coefficient. The residuals on these fits from the noise in the SERS spectra allow estimation of the concentration at which the highest peak would be discernible from the noise ([Supporting Information](#), Section 6). This provides an insight into the LOD for each analyte. Although, in practice, LODs are expected at slightly higher concentrations because several peaks need to clear the noise threshold (>0.03 cts·mW⁻¹·s⁻¹) for a spectrum to be distinct and recognizable ([Table 1](#)).

To confirm these estimated LODs are truly realistic, spectral changes at analyte concentrations near the LOD are compared

Table 1. Estimated LOD Based on the Hill–Langmuir Fit and Spectral Noise

analyte	concentration@signal > noise · 10 ⁻⁹ M
(2) Δ ⁹ -THC	0.34(±0.02)
(3) 5F-PB-22	0.05(±0.01)
(4) MMB-CHMICA	0.40(±0.09)
(5) 5F-AKB48	26.0(±0.03)

to the noise threshold (see [Supporting Information](#), Section 6 for details). The high reproducibility of the SERS spectra allows for the reference to be reliably subtracted from the raw data revealing spectral changes arising with the addition of the analyte and its carrier solvent, as shown for analyte (2:THC) in [Figure 7](#).

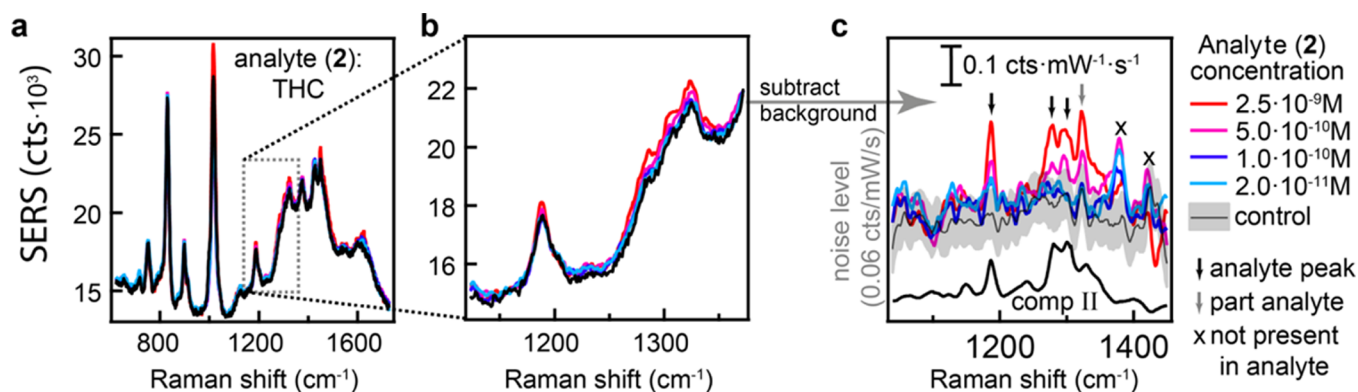


Figure 7. Validation of the LOD for analyte (2). (a) SERS spectra of CB[5]:AuNP aggregates with four different analyte concentrations (2.5, 0.5, 0.1, and 0.02 nM). The zoomed-in region of interest showing small spectral changes. (c) SERS spectra with the background subtracted, showing peaks for analyte (2) exceeding the noise threshold for 2.5 and 0.5 nM concentrations (arrows).

At 2.5 and 0.5 nM, the analyte peaks are still recognizable and exceed the noise threshold (Figure 7c), while at 0.1 nM, the signal has dropped into the noise. This is in good agreement with the derived LOD of 0.34 nM, showing that using the Hill–Langmuir fit with PCA scores is a suitable technique to approximate LODs. Such low LODs are typically the preserve of immunoassay SERS substrates tailored to detect a specific analyte.²⁰ Interestingly, a higher LOD is observed for compound (5) and is paired with a higher Hill coefficient (see Supporting Information, Table S2), indicating a stronger competitive binding occurs for this analyte. Exploring in detail what determines this difference in the LOD will further push understanding of the complex interactions present in self-assembled plasmonic nanogaps and is the subject of the ongoing research. However, it is clear that the chemical environment of plasmonic gaps can be exploited for interstitial analyte incorporation and that eliminating excess binding sites has a drastic effect on improving the LODs. On this basis, new strategies can be developed for existing substrates to remove or passivate excess binding. Such strategies can, for example, involve multiple washing steps to remove excess binding sites or adding ions or large molecules to block these sites, leaving only hotspots exposed.

CONCLUSIONS

We have demonstrated an interstitial analyte incorporation mechanism in self-assembled colloidal SERS substrates and used it to show the effects of analyte “theft” by indiscriminate binding on the LOD. We have shown that for THC and all three tested synthetic analogues, weaker binding of molecular spacers results in higher SERS signals and lower LODs, reaching subnanomolar concentrations. These findings highlight that for SERS-based detection of analytes, at very low concentrations, indiscriminate binding of target molecules should be eliminated where possible, as this has a detrimental effect on signal strengths and when successful can increase the LOD by more than an order of magnitude.

METHODS

Concentration Series. THC (1 mg/mL in methanol) and methyl viologen dichloride were purchased from Sigma-Aldrich, the synthetic analogues 3–5 were provided by Tic Tac Communications, and all chemicals were used as received. The different analyte concentrations were prepared by volumetric dilution of analytes using either water (for MV²⁺) or methanol (laboratory reagent grade, Fisher Scientific)

as the solvent. Vials containing the diluted analyte concentrations were sealed and used within 1 h of preparation to minimize effects of solvent evaporation.

Formation of SERS Substrates. 60 nm AuNP suspensions were purchased from BBI Solutions (citrate capped, optical density OD1) and stored at 7 °C. Prior to use, the AuNP suspension was allowed to reach room temperature. CB[*n*] molecular spacers were synthesized and separated according to the procedure described in ref 25. To induce self-assembly, 7 μL of a 1 mM solution of CB[*n*] was added to the bottom of a black polystyrene 96-well plate (Thermo Fisher Scientific). AuNP suspension (300 μL) was added and allowed to aggregate for 10 min.

Analyte Detection. The CB[5], CB[6], CB[7], and CB[8] concentration series were measured using the same stock solutions, freshly prepared from a 1 mg/mL solution in methanol using volumetric dilution with a suitable carrier solvent (methanol for the synthetic cannabinoids and water for methyl viologen). Specifically, 1 mL of analyte (2) at 1 mg/mL in MeOH was added to an empty 5 mL volumetric flask and filled to the appropriate volume using MeOH. The new concentration in the flask (now, 0.2 mg/mL) was stored in a sealed container and 1 mL was drawn for the next dilution step. For SERS measurements, 20 μL of analyte solution was added to the aggregated suspension, mixed, and allowed to homogenize for 2 more minutes. SERS spectra were recorded on a commercial Renishaw Raman setup using either a 532, a 633, or a 785 nm laser, with typical quantitative measurements taken using a 785 nm laser at 119 mW, by combining 3 iterations with 10 s integration time. For focusing and collection, a 5 × 0.15 NA Olympus objective was used giving an estimated spot size of 0.4 mm³. To demonstrate reproducibility, typical measurements were performed at least in threefold, meaning three unique samples were created by combining CB[*n*] and AuNPs and adding the desired analyte concentration from a stock solution.

Principal Component Analysis. Prior to PCA, a linear background was subtracted from each of the spectra using the lowest point in the spectra. The WaveMetrics Igor implementation of PCA was used to calculate the loading plots and scores for each of the components. The PCA results were obtained as described in ref 36.

FDTD Simulations. FDTD simulations were performed using Lumerical FDTD Solutions v8.12. The AuNP chains were modeled as linear assemblies of core–shell spheres with a core diameter of 60 nm of Au and a dielectric shell of 0.9 nm with a refractive index of 1.45. The dielectric function of gold was taken from Johnson and Christy. The structure was illuminated with a broadband plane wave (TFSF source) polarized along the chain length. The scattering and near-field intensities were obtained from the inbuilt cross-section and near-field monitors. The narrow gaps of the plasmonic chains were simulated by using multiple meshing of the narrow gaps and nanoparticles. The calculations were converged at 0.3 nm meshing for the gaps along the dimer axis of the NPs and with $dx = dy = dz = 1$ nm meshing

throughout the NP volume. Care was taken to ensure there were no staircasing artifacts in defining the curved surface of nanoparticles. We have previously shown the importance of meshing in the accurate determination of field volumes and their contribution to near fields.⁴⁴

DFT Calculations. The gas phase and subsequent continuum solvent geometry optimizations of the complexes (THC@CB[*n*], *n* = 5–8), host (CB[*n*], *n* = 5–8), and guest (THC) molecules were performed using the hybrid B3LYP exchange–correlation functional in combination with the split-valence double-zeta polarized basis set, 6-31G* and including the Grimme's D3 dispersion correction with Becke–Johnson damping.⁴⁵ Continuum solvent geometry optimizations were performed using the SMD continuum models parametrized for water. The gas phase potential energies of the THC@CB[*n*], *n* = 5–8 complexes were corrected for the basis set superposition error, which is significant because of the incompleteness of the present basis set. For the accurate description of the low frequency modes, an ultrafine DFT integration grid was used. No symmetry restrictions were imposed during the geometry optimization procedure. Frequency calculations with the SMD solvent model⁴⁶ were performed at the same level of theory to obtain the association Gibbs free energies, $G_0^{\text{RRHO/QH}}(1)$ and enthalpies, $H_0^{\text{RRHO}}(1)$ in the rigid rotor/harmonic oscillator (RRHO) and quasi-harmonic (mixture of RRHO and free rotor vibrational entropies along with the translational entropy correction based on the free space accessible to the solute)^{47,48} (QH) approximation and including zero-point vibrational energy at 298 K and 1 atm. Final continuum solvent solution phase association Gibbs free energies ($\Delta G_{\text{bind}}^{\text{RRHO/QH}}$) and enthalpies ($\Delta H_{\text{bind}}^{\text{RRHO/QH}}$) were calculated by adding the counterpoise correction, $\delta E^{\text{CP}}(\text{g})$

$$\Delta G_{\text{bind}}^{\text{RRHO/QH}} = \Delta G_0^{\text{RRHO/QH}}(1) + \delta E^{\text{CP}}(\text{g})$$

$$\Delta H_{\text{bind}}^{\text{RRHO/QH}} = \Delta H_0^{\text{RRHO/QH}}(1) + \delta E^{\text{CP}}(\text{g})$$

where Δ represents that the supramolecular approach $\Delta X = X(\text{complex}) - X(\text{host}) - X(\text{guest})$ has been used. The association free energies are summarized in Table S1. All standard DFT calculations were performed by using the Gaussian 09⁴⁹ ab initio program package.

Free Energy Profiles of Association. MD simulations were performed with the NAMD 2.9⁵⁰ program using the CHARMM36⁵¹ force field. The THC@CB[*n*], *n* = 5–8 complexes were solvated in a pre-equilibrated TIP3P cubic water box of edge 65 Å. The resulting systems contain 8689, 8685, 8669, and 8660 H₂O molecules for *n* = 5, 6, 7, and 8, CB[*n*] analogues, respectively. Our MD protocol consisted of: (1) energy minimization over 15 000 steps; (2) equilibration over 1 ns in the *NPT* ensemble (*p* = 1.01325 bar and *T* = 303.15 K) with the RMSD of heavy atoms in CB[*n*], *n* = 5–8 and THC constrained to their initial position using a force constant of 1 kcal/(mol·Å²); (3) 2 ns run in the *NPT* ensemble; (4) US production runs of 5 ns in the *NPT* ensemble for each umbrella window with a spring constant of 100 kcal/(mol·Å²). Temperature and pressure were held constant at 303.15 K and 1 atm, respectively. A constant temperature was set by a Langevin thermostat with a damping coefficient of 1 ps⁻¹. All the bonds and angles involving hydrogen atoms were constrained by the SHAKE⁵² algorithm. We used the particle mesh Ewald method⁵³ for the long-range electrostatics in combination with a 12 Å cutoff for the evaluation of the nonbonded interactions. Trajectories were run with a time step of 2 fs and the collective variable employed in US was printed out in each step and used for the analysis. The umbrella bias for the host–guest association process was defined as the distance between COM of CB[*n*], *n* = 5–8 and the COM of the THC ligand. We used the dynamic histogram analysis method⁵⁴ to compute the free energy profiles along the association coordinate.

■ ASSOCIATED CONTENT

Supporting Information

The Supporting Information is available free of charge on the ACS Publications website at DOI: 10.1021/acssensors.9b01484.

High resolution FDTD modeling of the field enhancement and the resulting SERS intensity probability distribution; example calculation of analyte theft in a colloidal substrate; DFT calculations for the binding energies between THC and CB[*n*]; step-by-step analysis of the performed PCA analysis; demonstration of analyte identification using a simple Pearson correlation and comparisons to bulk powder spectra; and explanation about the reproducibility and noise estimation of the system and Langmuir–Hill fit parameters (PDF)

■ AUTHOR INFORMATION

Corresponding Author

*E-mail: jjb12@cam.ac.uk.

ORCID

István Szabó: 0000-0002-3700-3614

Rohit Chikkaraddy: 0000-0002-3840-4188

Steven J. Barrow: 0000-0001-6417-1800

Oren A. Scherman: 0000-0001-8032-7166

Edina Rosta: 0000-0002-9823-4766

Jeremy J. Baumberg: 0000-0002-9606-9488

Notes

The authors declare no competing financial interest.

Source data can be found at <https://doi.org/10.17863/CAM.44570>.

■ ACKNOWLEDGMENTS

We acknowledge financial support from EPSRC Grants (EP/L027151/1, EP/L015978/1, and EP/N020669/1) and the European Research Council grant BioNet 757850. B.d.N acknowledges support from the Leverhulme Trust and the Isaac Newton Trust, C.C. acknowledges support from NPL (PO443073), R.C. acknowledges support from the Dr. Manmohan Singh scholarship from St. John's College, M.K. thanks the European Commission for a Marie Skłodowska-Curie Fellowship (SPARCLES, 7020005), and S.J.B. thanks the European Commission for a Marie Skłodowska-Curie Fellowship (NANOSPHERE, 658360). D.B.G. acknowledges support from the EPSRC (EP/L015889/1). We thank Sheila Hardwick from the Home Office for her advice and help during the initial stages of the project.

■ REFERENCES

- (1) Cialla, D.; März, A.; Böhme, R.; Theil, F.; Weber, K.; Schmitt, M.; Popp, J. Surface-Enhanced Raman Spectroscopy (SERS): Progress and Trends. *Anal. Bioanal. Chem.* **2012**, *403*, 27–54.
- (2) Sharma, B.; Fernanda Cardinal, M.; Kleinman, S. L.; Greenelch, N. G.; Frontiera, R. R.; Blaber, M. G.; Schatz, G. C.; Van Duyne, R. P. High-Performance SERS Substrates: Advances and Challenges. *MRS Bull.* **2013**, *38*, 615–624.
- (3) Sharma, B.; Frontiera, R. R.; Henry, A.-I.; Ringe, E.; Van Duyne, R. P. SERS: Materials, Applications, and the Future. *Mater. Today* **2012**, *15*, 16–25.
- (4) Guerrini, L.; Graham, D. Molecularly-Mediated Assemblies of Plasmonic Nanoparticles for Surface-Enhanced Raman Spectroscopy Applications. *Chem. Soc. Rev.* **2012**, *41*, 7085–7107.

- (5) Schlücker, S. Surface-Enhanced Raman Spectroscopy: Concepts and Chemical Applications. *Angew. Chem., Int. Ed.* **2014**, *53*, 4756–4795.
- (6) Le Ru, E. C.; Etchegoin, P. G. Rigorous Justification of the |E|⁴ Enhancement Factor in Surface Enhanced Raman Spectroscopy. *Chem. Phys. Lett.* **2006**, *423*, 63–66.
- (7) Le Ru, E. C.; Meyer, M.; Etchegoin, P. G. Proof of Single-Molecule Sensitivity in Surface Enhanced Raman Scattering (SERS) by Means of a Two-Analyte Technique. *J. Phys. Chem. B* **2006**, *110*, 1944–1948.
- (8) Radziuk, D.; Moehwald, H. Prospects for Plasmonic Hot Spots in Single Molecule SERS towards the Chemical Imaging of Live Cells. *Phys. Chem. Chem. Phys.* **2015**, *17*, 21072–21093.
- (9) Le Ru, E. C.; Grand, J.; Sow, I.; Somerville, W. R. C.; Etchegoin, P. G.; Treguer-Delapierre, M.; Charron, G.; Félij, N.; Lévi, G.; Aubard, J. A Scheme for Detecting Every Single Target Molecule with Surface-Enhanced Raman Spectroscopy. *Nano Lett.* **2011**, *11*, 5013–5019.
- (10) McNay, G.; Eustace, D.; Smith, W. E.; Faulds, K.; Graham, D. Surface-Enhanced Raman Scattering (SERS) and Surface-Enhanced Resonance Raman Scattering (SERRS): A Review of Applications. *Appl. Spectrosc.* **2011**, *65*, 825–837.
- (11) Kasera, S.; Herrmann, L. O.; Barrio, J. del; Baumberg, J. J.; Scherman, O. A. Quantitative Multiplexing with Nano-Self-Assemblies in SERS. *Sci. Rep.* **2014**, *4*, 6785.
- (12) Kasera, S.; Biedermann, F.; Baumberg, J. J.; Scherman, O. A.; Mahajan, S. Quantitative SERS Using the Sequestration of Small Molecules Inside Precise Plasmonic Nanoconstructs. *Nano Lett.* **2012**, *12*, 5924–5928.
- (13) Le Ru, E. C.; Etchegoin, P. G.; Meyer, M. Enhancement Factor Distribution around a Single Surface-Enhanced Raman Scattering Hot Spot and Its Relation to Single Molecule Detection. *J. Chem. Phys.* **2006**, *125*, 204701.
- (14) Fang, Y.; Seong, N.-H.; Dlott, D. D. Measurement of the Distribution of Site Enhancements in Surface-Enhanced Raman Scattering. *Science* **2008**, *321*, 388–392.
- (15) Yonzon, C. R.; Haynes, C. L.; Zhang, X.; Walsh, J. T.; Van Duyne, R. P. A Glucose Biosensor Based on Surface-Enhanced Raman Scattering: Improved Partition Layer, Temporal Stability, Reversibility, and Resistance to Serum Protein Interference. *Anal. Chem.* **2004**, *76*, 78–85.
- (16) Alharbi, O.; Xu, Y.; Goodacre, R. Detection and Quantification of the Opioid Tramadol in Urine Using Surface Enhanced Raman Scattering. *Analyst* **2015**, *140*, 5965–5970.
- (17) Alvarez-Puebla, R. A.; Liz-Marzán, L. M. Traps and Cages for Universal SERS Detection. *Chem. Soc. Rev.* **2012**, *41*, 43–51.
- (18) Alharbi, O.; Xu, Y.; Goodacre, R. Simultaneous Multiplexed Quantification of Nicotine and Its Metabolites Using Surface Enhanced Raman Scattering. *Analyst* **2014**, *139*, 4820–4827.
- (19) Bantz, K. C.; Meyer, A. F.; Im, Ö.; Lindquist, N. C.; Oh, S.-H.; Haynes, C. L.; Lindquist, C.; Oh, S.-H.; Haynes, L. Recent Progress in SERS Biosensing. *Phys. Chem. Chem. Phys.* **2011**, *13*, 11551–11567.
- (20) Wang, G.; Park, H.-Y.; Lipert, R. J.; Porter, M. D. Mixed Monolayers on Gold Nanoparticle Labels for Multiplexed Surface-Enhanced Raman Scattering Based Immunoassays. *Anal. Chem.* **2009**, *81*, 9643–9650.
- (21) Jones, C. L.; Bantz, K. C.; Haynes, C. L. Partition Layer-Modified Substrates for Reversible Surface-Enhanced Raman Scattering Detection of Polycyclic Aromatic Hydrocarbons. *Anal. Bioanal. Chem.* **2009**, *394*, 303–311.
- (22) Xie, Y.; Wang, X.; Han, X.; Xue, X.; Ji, W.; Qi, Z.; Liu, J.; Zhao, B.; Ozaki, Y. Sensing of Polycyclic Aromatic Hydrocarbons with Cyclodextrin Inclusion Complexes on Silver Nanoparticles by Surface-Enhanced Raman Scattering. *Analyst* **2010**, *135*, 1389–1394.
- (23) Abalde-Cela, S.; Hermida-Ramón, J. M.; Contreras-Carballada, P.; Cola, L. D.; Guerrero-Martínez, A.; Alvarez-Puebla, R. A.; Liz-Marzán, L. M. SERS Chiral Recognition and Quantification of Enantiomers through Cyclodextrin Supramolecular Complexation. *ChemPhysChem* **2011**, *12*, 1529–1535.
- (24) Pande, S.; Ghosh, S. K.; Praharaj, S.; Panigrahi, S.; Basu, S.; Jana, S.; Pal, A.; Tsukuda, T.; Pal, T. Synthesis of Normal and Inverted Gold–Silver Core–Shell Architectures in β -Cyclodextrin and Their Applications in SERS. *J. Phys. Chem. C* **2007**, *111*, 10806–10813.
- (25) Barrow, S. J.; Kasera, S.; Rowland, M. J.; del Barrio, J.; Scherman, O. A. Cucurbituril-Based Molecular Recognition. *Chem. Rev.* **2015**, *115*, 12320–12406.
- (26) Taylor, R. W.; Lee, T.-C.; Scherman, O. A.; Esteban, R.; Aizpurua, J.; Huang, F. M.; Baumberg, J. J.; Mahajan, S. Precise Subnanometer Plasmonic Junctions for SERS within Gold Nanoparticle Assemblies Using Cucurbit[n]uril “Glue. *ACS Nano* **2011**, *5*, 3878–3887.
- (27) Sigle, D. O.; Kasera, S.; Herrmann, L. O.; Palma, A.; de Nijs, B.; Benz, F.; Mahajan, S.; Baumberg, J. J.; Scherman, O. A. Observing Single Molecules Complexing with Cucurbit[7]uril through Nanogap Surface-Enhanced Raman Spectroscopy. *J. Phys. Chem. Lett.* **2016**, *7*, 704–710.
- (28) Chen, T.; Wang, H.; Chen, G.; Wang, Y.; Feng, Y.; Teo, W. S.; Wu, T.; Chen, H. Hotspot-Induced Transformation of Surface-Enhanced Raman Scattering Fingerprints. *ACS Nano* **2010**, *4*, 3087–3094.
- (29) Lee, A.; Andrade, G. F. S.; Ahmed, A.; Souza, M. L.; Coombs, N.; Tumarkin, E.; Liu, K.; Gordon, R.; Brolo, A. G.; Kumacheva, E. Probing Dynamic Generation of Hot-Spots in Self-Assembled Chains of Gold Nanorods by Surface-Enhanced Raman Scattering. *J. Am. Chem. Soc.* **2011**, *133*, 7563–7570.
- (30) Chen, T.; Du, C.; Tan, L. H.; Shen, Z.; Chen, H. Site-Selective Localization of Analytes on Gold Nanorod Surface for Investigating Field Enhancement Distribution in Surface-Enhanced Raman Scattering. *Nanoscale* **2011**, *3*, 1575–1581.
- (31) Lee, T.-C.; Scherman, O. A. Formation of Dynamic Aggregates in Water by cucurbit[5]uril Capped with Gold Nanoparticles. *Chem. Commun.* **2010**, *46*, 2438–2440.
- (32) Esteban, R.; Taylor, R. W.; Baumberg, J. J.; Aizpurua, J. How Chain Plasmons Govern the Optical Response in Strongly Interacting Self-Assembled Metallic Clusters of Nanoparticles. *Langmuir* **2012**, *28*, 8881–8890.
- (33) Taylor, R. W.; Esteban, R.; Mahajan, S.; Aizpurua, J.; Baumberg, J. J. Optimizing SERS from Gold Nanoparticle Clusters: Addressing the Near Field by an Embedded Chain Plasmon Model. *J. Phys. Chem. C* **2016**, *120*, 10512–10522.
- (34) Romero, I.; Aizpurua, J.; Bryant, G. W.; García De Abajo, F. J. Plasmons in Nearly Touching Metallic Nanoparticles: Singular Response in the Limit of Touching Dimers. *Opt. Express* **2006**, *14*, 9988–9999.
- (35) Carnegie, C.; Chikkaraddy, R.; Benz, F.; de Nijs, B.; Deacon, W. M.; Horton, M.; Wang, W.; Readman, C.; Barrow, S. J.; Scherman, O. A.; et al. Mapping SERS in CB: Au Plasmonic Nanoaggregates. *ACS Photonics* **2017**, *4*, 2681–2686.
- (36) de Nijs, B.; Kamp, M.; Szabó, I.; Barrow, J.; Benz, F.; Wu, G.; Carnegie, C.; Chikkaraddy, R.; Wang, W.; Deacon, W.; et al. Smart Supramolecular Sensing with Cucurbit[N]Urils: Probing Hydrogen Bonding with SERS. *Faraday Discuss.* **2017**, *205*, 505–515.
- (37) Feilchenfeld, H.; Chumanov, G.; Cotton, T. M. Photoreduction of Methylviologen Adsorbed on Silver. *J. Phys. Chem.* **1996**, *100*, 4937–4943.
- (38) Karschner, E. L.; Schwilke, E. W.; Lowe, R. H.; Darwin, W. D.; Pope, H. G.; Herning, R.; Cadet, J. L.; Huestis, M. A. Do Δ^9 -tetrahydrocannabinol concentrations indicate recent use in chronic cannabis users? *Addiction* **2009**, *104*, 2041–2048.
- (39) Kikura-Hanajiri, R.; Uchiyama, N.; Kawamura, M.; Goda, Y. Changes in the Prevalence of Synthetic Cannabinoids and Cathinone Derivatives in Japan until Early 2012. *Forensic Toxicol.* **2013**, *31*, 44–53.
- (40) Spaderna, M.; Addy, P. H.; D’Souza, D. C. Spicing Things up: Synthetic Cannabinoids. *Psychopharmacology* **2013**, *228*, 525–540.

(41) Lindigkeit, R.; Boehme, A.; Eiserloh, I.; Luebbecke, M.; Wiggermann, M.; Ernst, L.; Beuerle, T. Spice: A Never Ending Story? *Forensic Sci. Int.* **2009**, *191*, 58–63.

(42) Namera, A.; Kawamura, M.; Nakamoto, A.; Saito, T.; Nagao, M. Comprehensive Review of the Detection Methods for Synthetic Cannabinoids and Cathinones. *Forensic Toxicol.* **2015**, *33*, 175–194.

(43) Behonick, G.; Shanks, K. G.; Firchau, D. J.; Mathur, G.; Lynch, C. F.; Nashelsky, M.; Jaskierny, D. J.; Meroueh, C. Four Postmortem Case Reports with Quantitative Detection of the Synthetic Cannabinoid, 5F-PB-22. *J. Anal. Toxicol.* **2014**, *38*, 559–562.

(44) Kongsuwan, N.; Demetriadou, A.; Chikkaraddy, R.; Benz, F.; Turek, V. A.; Keyser, U. F.; Baumberg, J. J.; Hess, O. Suppressed Quenching and Strong-Coupling of Purcell-Enhanced Single-Molecule Emission in Plasmonic Nanocavities. *ACS Photonics* **2018**, *5*, 186–191.

(45) Grimme, S.; Ehrlich, S.; Goerigk, L. Effect of the Damping Function in Dispersion Corrected Density Functional Theory. *J. Comput. Chem.* **2011**, *32*, 1456–1465.

(46) Ribeiro, R. F.; Marenich, A. V.; Cramer, C. J.; Truhlar, D. G. Use of Solution-Phase Vibrational Frequencies in Continuum Models for the Free Energy of Solvation. *J. Phys. Chem. B* **2011**, *115*, 14556–14562.

(47) Grimme, S. Supramolecular Binding Thermodynamics by Dispersion-Corrected Density Functional Theory. *Chem.—Eur. J.* **2012**, *18*, 9955–9964.

(48) Mammen, M.; Shakhnovich, E. I.; Deutch, J. M.; Whitesides, G. M. Estimating the Entropic Cost of Self-Assembly of Multiparticle Hydrogen-Bonded Aggregates Based on the Cyanuric Acid-Melamine Lattice. *J. Org. Chem.* **1998**, *63*, 3821–3830.

(49) Frisch, M.; Trucks, G.; Schlegel, H.; Scuseria, G.; Robb, M.; Cheeseman, J.; Scalmani, G.; Barone, V.; Mennucci, B.; Petersson, G. *Gaussian 09*, Revision D. 01; Gaussian, Inc., 2009.

(50) Phillips, J. C.; Braun, R.; Wang, W.; Gumbart, J.; Tajkhorshid, E.; Villa, E.; Chipot, C.; Skeel, R. D.; Kalé, L.; Schulten, K. Scalable Molecular Dynamics with NAMD. *J. Comput. Chem.* **2005**, *26*, 1781–1802.

(51) Huang, J.; MacKerell, A. D. CHARMM36 All-Atom Additive Protein Force Field: Validation Based on Comparison to NMR Data. *J. Comput. Chem.* **2013**, *34*, 2135–2145.

(52) Andersen, H. C. Rattle: A “velocity” Version of the Shake Algorithm for Molecular Dynamics Calculations. *J. Comput. Phys.* **1983**, *52*, 24–34.

(53) Darden, T.; York, D.; Pedersen, L. Particle Mesh Ewald: An N- $\log(N)$ Method for Ewald Sums in Large Systems. *J. Chem. Phys.* **1993**, *98*, 10089–10092.

(54) Rosta, E.; Hummer, G. Free Energies from Dynamic Weighted Histogram Analysis Using Unbiased Markov State Model. *J. Chem. Theory Comput.* **2015**, *11*, 276–285.